PHOTONICS Research

Higher-order valley vortices enabled by synchronized rotation in a photonic crystal

Rui Zhou,[1] Hai Lin,[1,5] Yanjie Wu,[1] Zhifeng Li,[1] Zihao Yu,[1] Y. Liu,[2,3,6] and Dong-Hui Xu[4]

[1]College of Physics Science and Technology, Central China Normal University, Wuhan 430079, China
[2]School of Physics and Electronic Sciences, Hubei University, Wuhan 430062, China
[3]Lanzhou Center for Theoretical Physics, Key Laboratory of Theoretical Physics of Gansu Province, Lanzhou University, Lanzhou 730000, China
[4]Department of Physics, Chongqing University, Chongqing 400044, China
[5]e-mail: linhai@mail.ccnu.edu.cn
[6]e-mail: yangjie@hubu.edu.cn

Received 6 December 2021; revised 22 February 2022; accepted 10 March 2022; posted 14 March 2022 (Doc. ID 452598); published 21 April 2022

Synchronized rotation of unit cells in a periodic structure provides a novel design perspective for manipulation of band topology. We then design a two-dimensional version of higher-order topological insulator (HOTI) by such rotation in a triangular photonic lattice with C_3 symmetry. This HOTI supports the hallmark zero-dimensional corner states and, simultaneously, the one-dimensional edge states. We also find that our photonic corner states carry chiral orbital angular momenta locked by valleys, whose wave functions are featured by the phase vortex (singularity) positioned at the maximal Wyckoff points. Moreover, when excited by a fired source with various frequencies, the valley topological states of both one-dimensional edges and zero-dimensional corners emerge simultaneously. Extendable to higher or synthetic dimensions, our paper provides access to a chiral vortex platform for HOTI realizations in the terahertz photonic system.

https://doi.org/10.1364/PRJ.452598

1. INTRODUCTION

With further development of photonic crystals (PhCs) armored by topological understanding for condensed matter, people have found miscellaneous photonic counterparts of topological phases [1–5]. Among them, the topological edge states generated on the interface between different topological phases promise superior features, such as robustly smooth transmission, backscattering suppression, and defect immunity despite rather strong perturbation of the local boundary. Following quantum Hall phases [2], more intricate topological phases, such as quantum spin Hall phases [3,5] and quantum valley Hall phases [4], are also invented in the context of analog PhC systems, the two of which, respectively, exploit the dichroism freedom by redefining pseudospin/valley concepts in classical wave setups. Such configurable symmetrical lattices, furthermore, provide easy access to topological crystalline insulators (TCIs), for example, those with synchronous rotation giving rise to high tunability in practical realization [6]. Specifically for a C_3 kagome lattice of broken inversion symmetry, distinct valley states will emerge in the first Brillouin zone (FBZ) and produce their Berry curvature of opposite values [4,7,8]. Such a valleytronics concept calls for bulk valley states locked to their chiralities, which are possible to couple into and out of communication devices, such as valley filters and valley sources, respectively [4,7–10].

Nevertheless, a concept of corner states from higher-order topology that is one further dimension lower than the edges in a two-dimensional (2D) setup [11–15] has added new bricks to the premise for topological information devices. Among the class of higher-order phases, one type of topology is measured by the fractional bulk polarization (or the position of Wannier centers) [15]. For instance, 0D corner states, other than the 1D edge ones, emerge in the second-order TCIs, whose spatial positions are associated with Wannier centers determined from the polarization value [16–19].

Peculiar to the classical analog for topological quantum physics, the spatial vortex, i.e., the wave function with an undefined phase in certain spatial locations, remains less explored in the context of topological photonics despite its mechanical power to manipulate macroparticles. The vortex flow of electromagnetic waves, also defined as the orbital angular momentum (OAM) of light, may open up new avenues to exert optical torques to matters in a noninvasive manner. In this paper, we will reveal such a possibility by designing a valley higher-order topological insulator (HOTI) in a triangular lattice with C_3 symmetry, which is fueled by synchronous rotation of each unit cell. By observing the phase of electric fields near K and K' points, we recognize a valley selection feature discussed previously [4]. We also find that the synchronous rotation

mechanism of unit cells induces a band inversion at valleys, which leads to a topological phase transition in our photonic system. This topological transition can be characterized by the extended 2D bulk polarization related to the Zak phase [15,20,21]. In the electric field of the valley HOTI, pointwise corner states are predicted by the 2D bulk polarization. Furthermore, not only does our proposed HOTI have a vortex edge state locked to one of the dichroic valleys [22,23], but also it supports a topologically corner state. Using chiral point sources of different frequencies, our simulations verify that the electromagnetic waves shape into high-quality corner states and robust edge states. Our idea can be extended to higher or synthetic dimensions, which contributes to an experimentally feasible platform for HOTI in the photonic vortex system [4,8,9,24–26].

2. THEORY AND MODEL

We propose a 2D PhC in a triangular lattice with $\mathcal{C}_{3v}$ symmetry, the unit cell of which is composed of six identical pure dielectric cylinders embedded in air as shown in the left panel of Fig. 1(a). Additionally, the maximal Wyckoff points in the unit cell are represented by labels o, p, and q in real space. The dielectric permittivity is $\varepsilon_d = 7.5$, a_0 is the lattice constant,

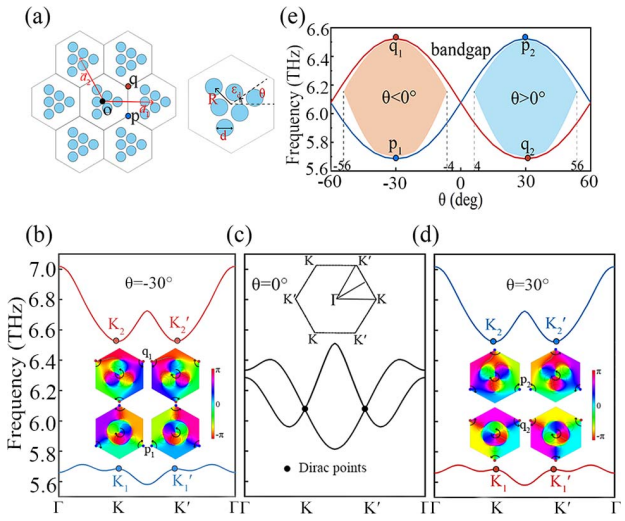

Fig. 1. (a) Left: Schematic of unrotated sampled PhC with lattice constant a_0 where the three positions in the $\mathcal{C}_3$ point group are labeled by o, p, q, respectively. Right: Rotated unit cell with θ as the rotation angle. (b)–(d) Dispersion bands of the valley PhC with $\theta = -30°, 0°$, and 30° [insets of (b) and (d) show the phase distributions]. Valley points of lower and higher frequencies are labeled by K_1 (K_1') and K_2 (K_2'), respectively. (b) When $\theta = -30°$, at the p_1 and q_1 points the phase distributions reveal that K_1 (K_1') and K_2 (K_2') have opposite chiralities, whose handedness is indicated by the black arrow in the insets. (c) When $\theta = 0°$, the Dirac points appear at points K and K' in the FBZ, and the inset shows the FBZ of the triangular lattice. (d) When $\theta = 30°$, K and K' valley points near the bandgap are reversed in frequency order at q_2 and p_2 compared to panel (b). (e) The blue and the red bands represent the frequency gap variation of the K valley when the unit cell rotates between −60° and +60° in a period. The crayon and orange shadings indicate the complete bandgap width of bands when rotating for different angles. Note that no complete gaps remain between −4° and +4°.

and $\mathbf{a}_1$ and $\mathbf{a}_2$ are the lattice vectors with cylinder diameter $d = 0.2a_0$, the lattice constants $a_0 = 50$ μm, and $a_0/R = 3.5$. The synchronous rotation angle of the dielectric cylinders in the unit cell is represented by θ, shown in the right panel of Fig. 1(a) with counterclockwise rotation as the positive direction of rotation whose maximum rotation angle is 60°.

In this paper, a finite element method is used to calculate the PhC dispersion and to solve for the related electric fields. In a $\mathcal{C}_3$-symmetric lattice, the photonic FBZ contains a pair of K and K' points in its vertices, which are named valley points [27,28] as shown in the Fig. 1(c) inset. Here, the valley states at K and K', connected by time-reversal (TR) symmetry [29,30], are both linearly dispersed, which are, hence, named Dirac points [31]. We only focus on the eigenstates near these two valley points and refer valleys K and K' to Dirac points throughout our whole paper to be succinct. *De facto*, there are more valley points with Dirac dispersion [cf. Fig. 6(b) in Appendix A]. Considering the transverse magnetic (TM) mode for simplicity, the band degeneracy at two Dirac points in Fig. 1(c) is levitated away from linear dispersion by rotating the dielectric cylinders in every unit, which are shown in Figs. 1(b) and 1(d). For the complete band diagram, see Appendix A. To be specific, when rotated away from the original lattice ($\theta = 0°$) in Fig. 1(c), the Dirac degeneracy is levitated to open a bandgap near the Dirac points. We define the lower- and higher-frequency states at K (K') as represented by K_1 (K_1') and K_2 (K_2'), respectively, in Figs. 1(b) and 1(d). When the unit cells are rotated counterclockwise $\theta = 30°$, two pairs of valley states are presented as insets in Fig. 1(d). In addition, these valley states in gap occupy chirality in the sense of circularly polarized OAM, which is manifested by the phase distribution of E_z, i.e., $\arg(E_z)$ [10,32]. For the K valley, the phases of K_1 and K_2 have opposite vortex chirality at the positions of p and q, respectively [denoted as p_1 and q_1 for $\theta = -30°$ and p_2 and q_2 for $\theta = +30°$ shown in the insets in Figs. 1(b) and 1(d)] and vice versa for the K' valley. With the opposite signs of θ, the frequency orders of the valleys corresponding to p and q positions are reverse as shown in Fig. 1(e), indicating a typical band inversion that leads to a topological phase transition [5]. The crayon and orange shadings in Fig. 1(e) mark out the complete bandgap width of the system during synchronous rotation of unit cells.

Let us focus on the properties of the K-valley state, i.e., K_1 and K_2 for its lower and higher band in frequency, respectively, whereas the counterparts for the K' valley can be deduced by TR symmetry (cf. Appendix B) [17,29,33]. We find that the photonic valley states are chiral in the sense of phase singularity, which can be readily seen from the electric fields in Fig. 2 where the top and bottom panels display the phase and amplitude distributions, respectively. In the positions of maximal Wyckoff [13] q and p, the electric amplitudes E_z vanish, and, thus, the phases become singular for the chiral valley states [34]. Note that in our PhC unit of $\mathcal{C}_3$ symmetry, it has three maximal Wyckoff positions: o at the center of the unit cell, and q and p at the vertices of it [cf. Fig. 1(a) and Appendix D]. The electric fields above reveal a typical feature of the vortex field, aligning in flow directions defined by time-averaged Poynting vectors $\mathbf{S} = \mathrm{Re}[\mathbf{E} \times \mathbf{H}^*]/2$ [35], which are represented by

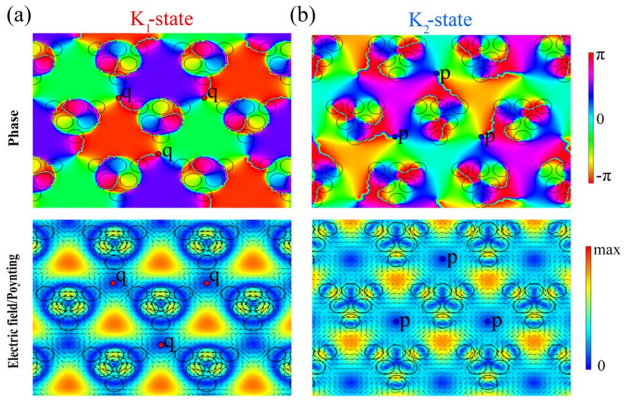

Fig. 2. Electric-field distribution $|E_z|(x,y)$ of the K-valley state (low-frequency K_1, high-frequency K_2) at positions p, q (p, q indicate positions with C_{3v} symmetry). Parameter: rotational angle $\theta = 30°$. The upper and lower panels, respectively, represent the valley phase and electric-field amplitude distribution of the large-period lattice, and the arrows in the lower panel indicate the corresponding time-averaged Poynting vector.

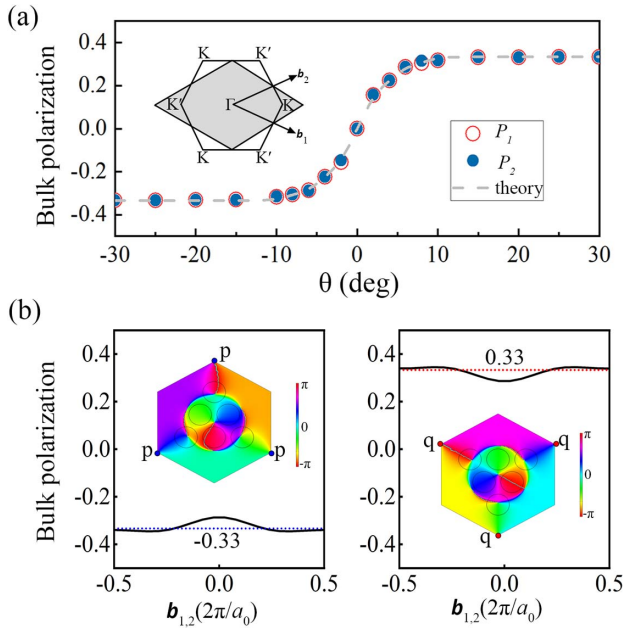

Fig. 3. (a) Bulk polarization changes when the unit cells rotate synchronously. Red circles for P_1, blue dots for P_2, dotted line for the theoretical calculation, and the inset for the schematic of the FBZ. (b) Left: When $\theta = -30°$, the polarization value along the wave-vector $\mathbf{b}_{1,2}$ direction $P_{1,2} = -1/3$ [bulk polarization $\mathbf{P} = (-1/3, -1/3)$] where the Wannier center in the unit cell aligns at the maximal Wyckoff positions p (blue dots in the inset). Right: When $\theta = 30°$, bulk polarization $\mathbf{P} = (1/3, 1/3)$ where the Wannier center is located at the maximal Wyckoff position q (red dots in the inset).

the arrows of the lower panels in Fig. 2. Therefore, we can control the chirality of the valley vortex by choosing the source chirality. Other than such valley-chirality locking, we also note that the K_1 state in E_z field distribution in Fig. 2(a) actually supports a whole circle of zero amplitude and singularity, and that in Fig. 2(b) a Y-type singularity curve, other than discrete singularity points. Recently, it has been suggested that the HOTI state can be evaluated by integrating the Berry connection in the FBZ, which is actually the Zak phase along the wave-vector direction [17,20,21,33]. The 2D Zak phase is connected to the fractional polarization through $\theta_i = 2\pi P_i$ for $i = 1, 2$ where its Zak phase or polarization is completely determined by the bulk property. In the 2D system, the bulk polarization is defined in terms of the Berry connection as [36]

$$P_i = -\frac{1}{(2\pi)^2}\int \mathrm{d}^2\mathbf{k}\,\mathrm{Tr}[\hat{\mathcal{A}}_i], \quad i = 1, 2, \tag{1}$$

with i indicating the component of $\mathbf{P}$ along the reciprocal lattice vector $\mathbf{b}_i$ ($i = 1, 2$). Here, $[A_i(\mathbf{k})]^{mn} = -i\langle u^m(\mathbf{k})\cdot|\partial k_i|u^n(\mathbf{k})\rangle$ is the Berry connection matrix where m and n run over occupied energy bands, and $|u^n(\mathbf{k})\rangle$ is the periodic Bloch function for the nth band with $\mathbf{k} = k_1\mathbf{b}_1 + k_2\mathbf{b}_2$ as the wave vector, where k_1, k_2 are integers. In reciprocal space, we can express the polarization in terms of the lattice vector via a numerical integration in Eq. (1). Then, the bulk polarization $\mathbf{P}$ of our PhC along $\mathbf{b}_{1,2}$ as illustrated in Fig. 3(a), equaling $(1/3, 1/3)$ or $(-1/3, -1/3)$ for $\theta \in (10°, 30°)$ and $\theta \in (-10°, -30°)$, indicates the topologically nontrivial phase, whereas $(0, 0)$ for $\theta \in (-10°, 10°)$ is a trivial phase (cf. Appendix C). In Fig. 3(a) the blue solid circles P_1 and the red hollow circles P_2 represent the polarization values in $\mathbf{b}_1$ and $\mathbf{b}_2$ directions. When $\theta \in (-10°, -30°)$, $\mathbf{P} = (-1/3, -1/3)$. This means that the Wannier center is located at the maximal Wyckoff position p as shown in Fig. 3(b). When $\theta \in (10°, 30°)$, $\mathbf{P} = (1/3, 1/3)$. Wannier centers are pinned to the maximal Wyckoff position q as shown in the Fig. 3(c) inset. As the pillars in the unit cells rotate, the topologically nontrivial polarization $\mathbf{P}$ varies from $(-1/3, -1/3)$ to $(1/3, 1/3)$. Consequently, the corner states associated with different polarization values appear at the maximal Wyckoff positions due to valley selection.

Therefore, our HOTI supports, thus, defined corner states in the bandgap, which appear at the maximal Wyckoff positions of the unit cell. Generally, in C_n-symmetric lattices, given a choice of unit cell, there exist special high-symmetry points (HSP) in the unit cell, which are called the maximal Wyckoff position (cf. Appendix D). As in Eq. (1), the nontrivial second-order topology and emergence of the valley-selective corner states are theoretically characterized by the nontrivial bulk polarizations and the associated Wannier centers. Here, the Wannier center refers to the center of the maximally localized Wannier function and for nontrivial polarization insulators, the Wannier center is located at the same position with the maximal Wyckoff position in the unit cell [12,13].

3. NUMERICAL RESULTS AND DISCUSSION

To investigate the concept of valley-selective HOTI, we construct nanodisks made of two types of triangular lattices with distinct polarizations. When $\theta \in (-30°, -10°)$, the eigenspectra of our nanodisk are shown in Fig. 4(a). The two colored curves indicate the eigenfrequency functions with θ for the two types of vertices [up-corner I (U-I) and up-corner II (U-II) for shorthand, respectively]. Here, we refer to the PhC with $\theta = -30°$ as the up-triangular PhC (UPC) and $\theta = 30°$ as the

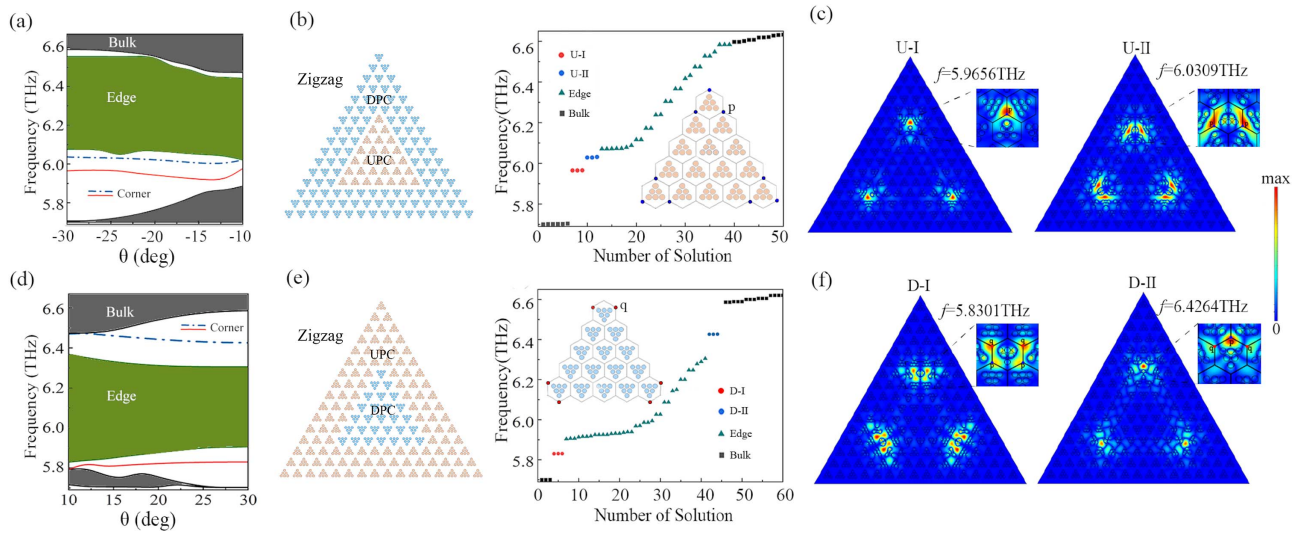

Fig. 4. Up-corner states and down-corner states in a triangular nanodisk with opposite polarization. (a) Eigenfrequency evolution spectrum when $\theta \in (-30°, -10°)$. Red solid line for U-I corner states, and blue dot-dashed line for U-II corner states. (b) Left panel: Schematic for zigzag edges with the DPC surrounding the UPC. Right panel: The UPC eigenspectra of the bulk-edge-corner states where the blue dots on the UPC indicate the positions of the Wannier centers selected by U-I and U-II corner states. (c) Electric-field distribution $|E_z|(x, y)$ of the U-I corner states at frequency $f = 5.9656$ THz and of the U-II corner state at frequency $f = 6.0309$ THz. (d) Eigenfrequency evolution spectra when $\theta \in (10°, 30°)$. Red solid line for D-I corner states, and blue dot-dashed line for D-II corner states. (e) Left panel: Schematic for zigzag edges with the UPC surrounding the DPC. Right panel: The DPC eigenfrequency distribution of the bulk-edge-corner states. The red dot of the DPC superunit model represents the Wannier center selected by the down-corner states. (f) Electric-field distribution of D-I and D-II corner states at frequencies $f = 5.8301$ and 6.4264 THz, respectively.

down-triangular PhC (DPC). A schematic for our simulation is shown in the left panel of Fig. 4(b) where the UPC is surrounded by the DPC to interface a zigzag edge mode. The eigenfrequencies of a bulk-edge corner in the UPC structure are shown in the right panel of Fig. 4(b) where the U-I and U-II corner states both are triply degenerate. In the insets of Figs. 4(b) and 4(e), Wannier centers are colored at the corners of the UPC structure. As the electric field shows in Fig. 4(c), Wannier center representation, illustrated by the red dots q in the UPC structure, reveals the valley selectivity of U-I corner states. Additionally, the blue dots q in the UPC structure reveal the valley selectivity of the U-II corner state. When $\theta \in (10°, 30°)$ the D-I and D-II corner states, respectively, appear below and above the edge state as shown in Fig. 4(d). From the eigenfrequency distribution of the DPC structure, we find that D-I and D-II corner states each also have three degenerate corner states, and the Wannier center configurations (in red dots) of the corner UPC structure are shown in the right panel of Fig. 4(e); whereas the electric field in Fig. 4(f) shows, Wannier centers (cf. p, q points in the picture) of the UPC and DPC are both fired by corner states. We speculate that in the DPC case [cf. the left panel of Fig. 4(e)] the zigzag boundary appears to disrupt and, hence, the corner states of the two models are excited mixedly at the same time. Moreover, the amplitude of the D-I corner electric field ($f = 5.8301$ THz) is higher than that of the D-II corner electric field ($f = 6.4264$ THz). For a further view of valley-selective corner states, we construct two kinds of hexagonal nanodisks forming armchair edges. Along some position of the armchair edge, the corner state of a polarization model can be excited separately, whose position is determined by its polarization value of the unit cell (cf. Appendix E). We remark that the valley selectivity behaves globally, which should apply beyond the UPC and the DPC cases here.

Now, we set up full-wave simulation to verify the corner and edge states above in one where the valley dependence of OAM chirality can be exploited to achieve unidirectional excitation of valley chiral states. In Fig. 5, we consider chiral line sources (in blue pentagrams where we choose an LCP OAM source) with a chiral phase, which are fired near the bottom of our PhC with three zigzag boundaries. By switching the source frequency, we can directly control the appearance of edge and corner states as shown in Figs. 5(a) and 5(b). In the superunit where the UPC is surrounded by the DPC, U-I and U-II corner states are, respectively, excited at frequencies $f = 5.9656$ THz and $f = 6.0309$ THz at the same frequencies as in Fig. 4(c). We note that corner states rely more sensitively on frequency parameters than edge ones do. Since the corner state transmits with loss, the electric amplitude of the corner state near the source remains higher than the further one. We choose frequency $f = 6.1700$ THz to fire the edge states, and our simulation shows that electromagnetic waves propagate smoothly along the interface even around sharp corners. It will promise new methods for streering electromagnetic waves along arbitrarily cornered pathways (cf. Appendix G). In the nanodisk where the DPC is surrounded by the UPC, D-I and D-II corner states are excited at $f = 5.8301$ THz and $f = 6.4264$ THz, respectively. In addition, the edge states are excited at

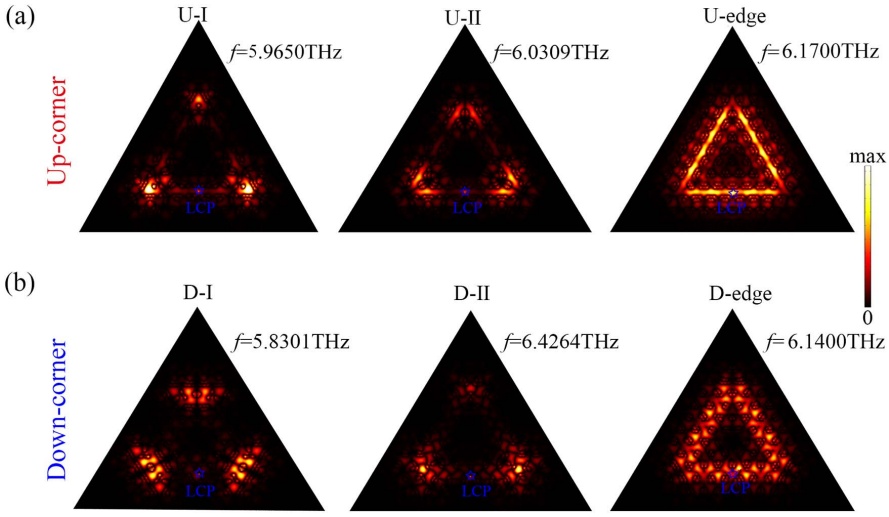

Fig. 5. Simulated electric-field $|E_z|(x, y)$ for a configuration consisting of the UPC [cf. inset of Fig. 4(b)] and the DPC [cf. inset of Fig. 4(e)]. The blue pentagram at the bottom of the configuration indicates a chiral OAM source. (a) Field distributions of the U-I and U-II corners and U edge where the UPC is surrounded by the DPC are excited by left-handed circularly polarized (LCP) chiral sources with frequencies $f = 5.9650, 6.0310, 6.1700$ THz. (b) Field distributions of D-I, D-II corners, and the D edge where the DPC is surrounded by the UPC are also excited by LCP sources with frequencies $f = 5.8301, 6.4260, 6.1400$ THz.

$f = 6.1400$ THz. Our results then show that corner states can be selectively excited by tuning the source frequency in addition to valley selection.

4. CONCLUSION

To summarize, we numerically realized a valley-type second-order topology due to unit-cell rotation characterized by the nontrivial bulk polarization. Specifically, the corner states are found to be valley dependent and, therefore, enable flexible manipulation on the wave localization. Thus, topological switches by valley selection of the corner states were numerically demonstrated in our paper. Our valley HOTI and the valley-selective corner states provide preliminary understanding on the interplay between the higher-order topology and the valley degree of freedom, which may find potential applications in valleytronics for future information carriers, such as waveguides, couplers, and topological circuit switches in the terahertz regime [24,30,37–42].

APPENDICES

Appendices A–G below are for the details of the complete band diagram, symmetry operation, polarization theoretical analysis, maximal Wyckoff positions, corner state distribution along armchair interfaces, and transport efficiency of the edge state along two boundary types.

APPENDIX A: COMPLETE BAND DIAGRAM

The nontrivial bandgaps were distributed in the range of 5.5–6.5 THz, i.e., seventh band, which is what we focused on in the main text. We then showed the complete band diagram of the PhCs for three rotation angles. When $\theta = -30°$ and $\theta = 30°$, four complete bandgaps were produced. The green regions indicated the nontrival bandgap, and the brown regions indicated the trivial bandgap as shown in Figs. 6(a) and 6(c). At $\theta = 0°$, bands 2, 3, 7, and 8 were closed in Fig. 6(b). Four Dirac points (phase-transition points) appeared at K and K', and the topological nontrivial bandgap disappeared. In the main text, we analyzed that bands 7 and 8 reversed in frequency order during rotation, and we noted that no edge states appeared between bands 1 and 2 by rotation of the unit cells.

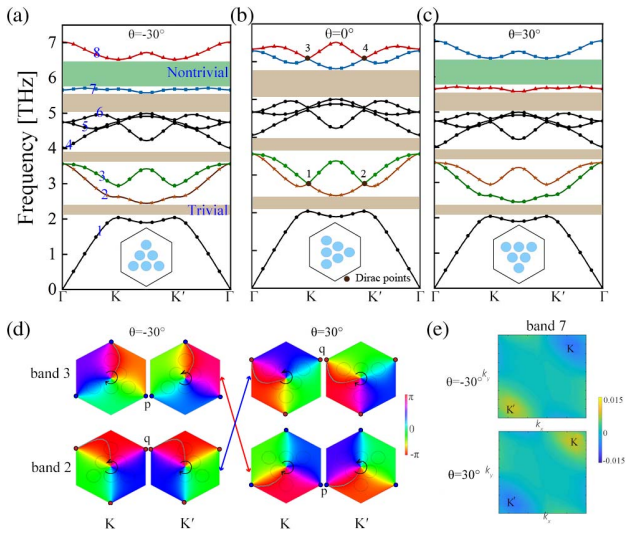

Fig. 6. TM mode dispersion diagrams when the PhC unit cell rotates for different angles. (a)–(c) When $\theta = -30°$ and $\theta = 30°$, four complete bandgaps are produced, the green regions indicate the nontrival bandgap, and the brown regions indicate the trival bandgap. (b) When $\theta = 0°$, bands 2, 3, 7, and 8 are closed. Four Dirac points (phase-transition points) appear at K and K', and the topological nontrivial bandgap disappears. (d) When $\theta = -30°$ and $\theta = 30°$, the phase distribution of bands 2 and 3 at points K and K'. (e) Berry curvature near K and K' for the 7th band.

Here, we focused on analyzing the properties of K and K' points in bands 2 and 3. At $\theta = -30°$ and $\theta = 30°$, we found the K-valley states had opposite vortex chirality, and vice versa for the K' valley shown in Fig. 6(d). With the opposite signs of θ, the frequency orders of the valleys corresponding to p and q states were reversed, indicating a typical band inversion that led to a topological phase transition. Additionally, there was no complete bandgap in bands 2 and 3, which, although, might still host topological edge states (not shown here). In the main text, we determined through the polarization value that the bandgap between bands 7 and 8 was nontrivial. Furthermore we numerically calculated the Berry curvature of band 7 according to its eigenstates and found the opposite sign of Berry curvature in different valleys as shown in Fig. 6(e). The Berry connection of the 7th band can be defined as [32]

$$\vec{A}(\vec{k}) \equiv i\langle u_{\vec{k}}|\nabla_{\vec{k}}|u_{\vec{k}}\rangle = i\oint_{\text{unitcell}} \mathrm{d}^2 r\epsilon(\vec{r})u^*_{\vec{k}}[\nabla_{\vec{k}}u_{\vec{k}}], \tag{A1}$$

where $u_{\vec{k}}$ is the electromagnetic fields, an asterisk denotes complex conjugation, and $\epsilon(\vec{r})$ is the spatial permittivity distribution. Note that the eigenstate amplitude was normalized such that $\langle u_{\vec{k}}|u_{\vec{k}}\rangle = 1$ and that phases of each eigenstate should be normalized by keeping the phase constant at one arbitrary point. The gauge-independent Berry curvature $\Omega(\vec{k})$ is obtained by

$$\Omega(\vec{k}) \equiv \nabla_{\vec{k}} \times \vec{A}(\vec{k}) = \frac{\partial A_y(\vec{k})}{\partial k_x} - \frac{\partial A_x(\vec{k})}{\partial k_y}. \tag{A2}$$

Figure 6(e) shows the Berry curvature near K and K' points of the 7th band for valley PhCs. The extreme Berry curvature is located at each of the two valley centers. Topological indices at K and K' valleys are defined as the integration of Berry curvature within half a BZ.

APPENDIX B: TR SYMMETRY AND ROTATION SYMMETRY

We first reviewed in concept TR symmetry (TRS), then rotation symmetry, and finally the interplay of the two of them. Using these constraints, we then constructed the complete set of invariants for C_3-symmetry insulators. Insulators in this class have TRS with a Bloch Hamiltonian satisfying [15]

$$\Theta h(\mathbf{k})\Theta^{-1} = h(-\mathbf{k}). \tag{B1}$$

Here, $\Theta = K$ is the TR operator, which consists only of complex conjugation K. The operator obeys $\Theta^2 = 1$. Acting on an energy eigenstate, we have

$$h(-\mathbf{k})\Theta|u^n_{\mathbf{k}}\rangle = \Theta h(\mathbf{k})|u^n_{\mathbf{k}}\rangle = \epsilon_n(\mathbf{k})\Theta|u^n_{\mathbf{k}}\rangle. \tag{B2}$$

Thus, $\Theta|u^n_{\mathbf{k}}\rangle$ is an eigenstate of $h(-\mathbf{k})$ with energy $\epsilon_n(\mathbf{k})$. This means that we can write the expansion,

$$\Theta|u^n_{\mathbf{k}}\rangle = \sum_m |u^m_{-\mathbf{k}}\rangle V^{mn}_{\mathbf{k}}, \tag{B3}$$

where

$$V^{mn}_{\mathbf{k}} = \langle u^m_{-\mathbf{k}}|\Theta|u^n_{\mathbf{k}}\rangle = \langle u^m_{-\mathbf{k}}|u^{n*}_{\mathbf{k}}\rangle \tag{B4}$$

is the unitary sewing (transformation) matrix. Using Eqs. (B2) and (B3), we write

$$h(-\mathbf{k})\Theta|u^n_{\mathbf{k}}\rangle = \epsilon_n(\mathbf{k})\Theta|u^n_{\mathbf{k}}\rangle = \epsilon_n(\mathbf{k})\sum_m |u^m_{-\mathbf{k}}\rangle V^{mn}_{\mathbf{k}}. \tag{B5}$$

Next, using Eqs. (B2) and (B3), we have

$$h(-\mathbf{k})\Theta|u^n_{\mathbf{k}}\rangle = h(-\mathbf{k})\sum_m |u^m_{-\mathbf{k}}\rangle V^{mn}_{\mathbf{k}} = \sum_m \epsilon_m(-\mathbf{k})|u^m_{-\mathbf{k}}\rangle V^{mn}_{\mathbf{k}} \tag{B6}$$

for every n. Furthermore, since the eigenstate forms an orthogonal basis, Eq. (B6) above implies that

$$V^{\mathrm{mn}}_{\mathbf{k}}[\epsilon_n(\mathbf{k}) - \epsilon_{\mathrm{m}}(-\mathbf{k})] = 0, \tag{B7}$$

and

$$V^{mn}_{\mathbf{k}^\star} = \langle u^m_{\mathbf{k}^\star}|u^{n*}_{\mathbf{k}^\star}\rangle, \tag{B8}$$

whereas for rotation symmetry, we proceed in a similar way to that for TRS. Rotation symmetry is expressed as

$$\hat{r}h(\mathbf{k})\hat{r}^\dagger = h(R\mathbf{k}). \tag{B9}$$

Here, $\hat{r}$ is the n-fold rotation operator, which obeys $\hat{r}^n = 1$. Acting on an energy eigenstate, we have

$$h(R\mathbf{k})\hat{r}|u^n_{\mathbf{k}}\rangle = \hat{r}h(\mathbf{k})|u^n_{\mathbf{k}}\rangle = \epsilon_n(\mathbf{k})\hat{r}|u^n_{\mathbf{k}}\rangle. \tag{B10}$$

Thus, $\hat{r}|u^n_{\mathbf{k}}\rangle$ is an eigenstate of $h(R\mathbf{k})$ with energy $\epsilon_n(\mathbf{k})$. We can, then, write the expansion,

$$\hat{r}|u^n_{\mathbf{k}}\rangle = \sum_m |u_{-\mathbf{k}}\rangle B^{mn}_{\mathbf{k}}, \tag{B11}$$

where

$$B^{mn}_{\mathbf{k}} = \langle u^m_{R\mathbf{k}}|\hat{r}|u^n_{\mathbf{k}}\rangle \tag{B12}$$

is the rotation sewing matrix. An analysis analogous to TRS leads to the following expression:

$$B^{mn}_{\mathbf{k}}[\epsilon_n(\mathbf{k}) - \epsilon_m(R\mathbf{k})] = 0 \tag{B13}$$

for every m and n. This means that the sewing matrix $B^{mn}_{\mathbf{k}}$ only connects states at K and $R\mathbf{k}$ having the same energy.

Invariant points under rotation with C_3 symmetry, in C_3-symmetric TCIs, there are only three threefold HSPs: K, K', and Γ. These points are shown in Fig. 7(b) for all the crystalline symmetries.

Finally, we inspect the interplay between TRS and rotation symmetry. The two operators commute

$$[\Theta, \hat{r}] = 0. \tag{B14}$$

Thus, on one hand, we have

$$\Theta(\hat{r}|u^l_{\mathbf{k}}\rangle) = \Theta\left(\sum_n |u^n_{R\mathbf{k}}\rangle B^{nl}_{\mathbf{k}}\right) = \sum_{m,n} |u^m_{-R\mathbf{k}}\rangle V^{mn}_{R\mathbf{k}} B^{nl*}_{\mathbf{k}}. \tag{B15}$$

On the other hand, we have

$$\hat{r}(\Theta|u^l_{\mathbf{k}}\rangle) = \hat{r}\left(\sum_m |u^n_{-\mathbf{k}}\rangle V^{nl}_{\mathbf{k}}\right) = \sum_{m,n} |u^m_{-R\mathbf{k}}\rangle B^{mn}_{-\mathbf{k}} V^{nl}_{\mathbf{k}}. \tag{B16}$$

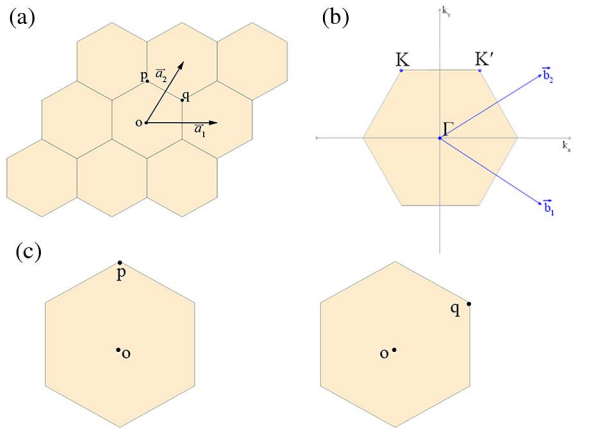

Fig. 7. (a) Schematic showing our choice of lattice vectors $\mathbf{a}_1, \mathbf{a}_2$ for C_3 TCIs. (b) BZ and reciprocal lattice vectors for C_3-symmetric crystals, $\mathbf{b}_1 = 2\pi(1, -1/\sqrt{3}), \mathbf{b}_2 = 2\pi(1, 1/\sqrt{3})$. FBZ of crystals with C_3 symmetries and their rotation invariant points; K and K' are threefold HSPs. (c) Three maximal Wyckoff positions in the C_3-symmetric: point o at the center of the unit cell and the points p, q at the corners of the unit cell.

In the last expression, we have used the fact that $R(-\mathbf{k}) = -R\mathbf{k}$. From these two expressions, we concluded that

$$\sum_n (V^{mn}_{R\mathbf{k}} B^{nl*}_{\mathbf{k}} - B^{mn}_{-\mathbf{k}} V^{nl}_{\mathbf{k}}) = 0 \tag{B17}$$

for all l, m. We consider points $\mathbf{k} = \mathbf{\Pi}$ such that

$$R\mathbf{\Pi} = \mathbf{\Pi},$$

in the BZ. Thus, if $V^{ml}_{\mathbf{\Pi}} \neq 0, r^{l*}_{\mathbf{\Pi}} = r^m_{-\mathbf{\Pi}}$, this is possible only if $\epsilon_m(-\mathbf{\Pi}) = \epsilon_l(\mathbf{\Pi})$. Thus, we have that under TRS,

$$\{r^n_{\mathbf{\Pi}}\} \overset{\text{TRS}}{=} \{r^{n*}_{-\mathbf{\Pi}}\}. \tag{B18}$$

In in C_3-symmetric TCIs, there are only three threefold HSPs: K, K' map into each other under TR. This implied that the rotation invariants defined obeyed $[K_2^{(3)}] \overset{C_3}{=} [K'_3]$.

APPENDIX C: QUANTIZATION OF POLARIZATION

In this appendix, we review the quantization of polarization due to C_n symmetry [15]. We denote the lattice vectors in real space as $\mathbf{a}_1, \mathbf{a}_2$ and the corresponding reciprocal lattice vectors in K space as $\mathbf{b}_1, \mathbf{b}_2$. The reciprocal lattice vectors satisfy

$$\mathbf{a}_i \cdot \mathbf{b}_j = 2\pi\delta_{ij}. \tag{C1}$$

Without loss of generality, we choose our lattice vectors and reciprocal lattice vectors for each symmetry to be those shown in Fig. 7. The conventional modern definition of polarization per unit cell in 2D crystals is

$$\mathbf{P} = -\frac{e}{S}\int_{\text{BZ}} \text{Tr}[\mathcal{A}(\mathbf{k})]\text{d}^2\mathbf{k}, \tag{C2}$$

where S is the area of the BZ and $\mathcal{A}$ is the Berry connection, which has components $\mathcal{A}^{\alpha\beta}(\mathbf{k}) = -i\langle u^\alpha(\mathbf{k})|\nabla_{\mathbf{k}}|u^\beta(\mathbf{k})\rangle$ defined at each K point in the BZ. We parameterize the BZ as $\mathbf{k} = s_1\mathbf{b}_1 + s_2\mathbf{b}_2$ so that the integral in Eq. (C2) is

$$\mathbf{P} = -e\int_0^1 \text{d}s_1 \int_0^1 \text{d}s_2 \text{Tr}[\mathcal{A}(s_1\mathbf{b}_1 + s_2\mathbf{b}_2)], \tag{C3}$$

where the determinant of the Jacobian matrix that transforms the variables of integration from $\text{d}k_x\text{d}k_y$ to $\text{d}s_1\text{d}s_2$ cancels the area of the FBZ. We define the quantity,

$$\mu_i \equiv -\frac{e}{2\pi}\int_0^1 \text{d}s_1 \int_0^1 \text{d}s_2 \text{Tr}[\mathcal{A}(s_2\mathbf{b}_2 + s_1\mathbf{b}_1)] \cdot \mathbf{b}_i, \tag{C4}$$

so that the projection of polarization along the reciprocal lattice vector $\mathbf{b}_i$ is

$$\mathbf{P} \cdot \mathbf{b}_i = 2\pi\mu_i. \tag{C5}$$

In real space, we can express the polarization in terms of lattice vectors, $\mathbf{P} = (p_1\mathbf{a}_1 + p_2\mathbf{a}_2)$ modulo integer linear combinations of lattice vectors. Following Eq. (C1), the projection of $\mathbf{P}$ along the reciprocal lattice vector is

$$\mathbf{P} \cdot \mathbf{b}_i = (p_1\mathbf{a}_1 \cdot \mathbf{b}_i + p_2\mathbf{a}_2 \cdot \mathbf{b}_i) = 2\pi p_i. \tag{C6}$$

Therefore,

$$p_1 = \mu_1 \mod e, \quad p_2 = \mu_2 \mod e. \tag{C7}$$

e is the electronic charge. Now, we analyze the role of rotation symmetries. Under a rotation operation $\hat{r}_n$, the lattice vectors transform as $\mathbf{a}'_i = T^{ij}_n\mathbf{a}_j$ (in the following, we assume the summation over repeated indices). The polarization becomes

$$\mathbf{P} = p_i\mathbf{a}_i \to p_i T^{ij}_n \mathbf{a}_j. \tag{C8}$$

If the model is C_n symmetric, the change in polarization after a C_n rotation can only be multiples of lattice vectors,

$$\mathbf{P} = p_i\mathbf{a}_i \to (p_i + n_i)\mathbf{a}_i, \tag{C9}$$

where $n_i \in \mathbb{Z}e, i = 1, 2$. Comparing Eqs. (C8) and (C9), we find the constraints on the polarization due to rotation symmetry,

$$p_j T^{ji}_n = p_i + n_i. \tag{C10}$$

Without loss of generality, we choose the lattice vectors for C_3 symmetric TCIs to be $\mathbf{a}_1 = (1, 0)$ $\mathbf{a}_2 = (1/2, \sqrt{3}/2)$ [see Fig. 7(b)]. The polarization components,

$$p_1 = \frac{n_2 - n_1}{3}, \quad p_2 = -\frac{2n_2 + n_1}{3}, \text{ for } \mathcal{C}_3 \text{ symmetry.} \tag{C11}$$

Since p_1, p_2 are defined as mod e, the constraints from the above equations imply that with C_3 symmetry, p_1, p_2 are quantized to be $0, e/3, 2e/3$, and the difference of the two polarization components $p_1 - p_2$ is a multiple of the integer charge n_2. Therefore, the two polarization components are the same,

$$p_1 = p_2 \mod e, \quad \text{for } C_3 \text{ symmetry.} \tag{C12}$$

The quantization of the polarization indicates that with nontrivial polarization, the center of negative charges coincides with maximal Wyckoff positions in each unit cell as shown in Fig. 7(c). In C_3-symmetric TCIs, the only possible nontrivial polarizations are $(e/3, e/3)$ and $(2e/3, 2e/3)$ with the center of negative charges located at the maximal Wyckoff position p or q, respectively.

APPENDIX D: UNIT CELLS AND MAXIMAL WYCKOFF POSITIONS

In C_n-symmetric lattices, given a choice of unit cell, there were special high-symmetry points within the unit cell, called maximal Wyckoff positions, that were invariant under rotations (about the center of the unit cell) up to lattice translations. Let us take the C_3 symmetric lattice as an example (Fig. 7). In Figs. 7(a) and 7(c), we have three maximal Wyckoff positions: the C_3-symmetric point o at the center of the unit cell and the C_3-invariant points p, q at the corners of the unit cell [15].

APPENDIX E: SELECTION OF VALLEY HOTI CORNER STATES

Cutting the C_3 lattice structure in different directions, at least, two types of boundaries can be formed: the zigzag and the armchair types. In the eigenmodes, the UPC and DPC are bounded by each other to create edges [4]. To investigate the valley-locking property in our valley HOTI, we constructed two types of boundary structures with zigzag and armchair edges. The valley-selection property of HOTI in the zigzag boundary was shown in the main text where the U-II corner states were induced by long-range interactions of the unit cell [25] as shown in Fig. 4(d).

The valley selectivity was further manifested in the armchair edges where the corner states surprisingly only emerged at three (out of six) corners as shown in Figs. 8(a), 8(c), 8(d), 8(e), 8(f), and 8(g). In the UPC case, the eigenfrequencies of U-I and U-II corner states were represented by blue and red dots, and the brown dots indicated that there were corner states at the edge of the model. Observing the electric field of the U-corner states, it was found that the corners appeared in the blue (red) positions [cf. the inset of Fig. 8(a)] as shown in Figs. 8(b) and 8(c). It is worth noting that the corner state only appeared at the Wannier center with a polarization of $\mathbf{P} = (-1/3, -1/3)$ as shown in Figs. 8(c) and 8(d). In the DPC case, we found the frequencies of D-I and D-II corner states were the same as that of U-I and U-II corner states. It was also found that the corner state of the polarization of $\mathbf{P} = (1/3, 1/3)$ structure was excited alone. Whereas the D-I corner states only appeared in the blue positions [cf. inset of Fig. 8(e)], the D-II corner states only appeared in the red positions as shown in Figs. 8(g) and 8(h). In short, in the armchair-type model, the corner state of a polarization model was excited separately, whose position was determined by its polarization value of the unit cell.

APPENDIX F: THE BAND STRUCTURES OF NANORIBBON SUPERCELLS

In this appendix, we calculate the projected band of the ribbon surpercells for our valley photonic crystal (VPC). Consider four types of supercells, comprising the zigzag and armchair interfaces between the UPC and the DPC. From calculation, we know that in the trivial bandgap between bands 1 and 2, rotation of unit cells cannot induce topological edge states. Here, we focus on the edge states of the nontrivial bandgap between band 7 and band 8 [cf. Figs. 6(a)–6(c)]. In the nontrivial bandgap, the black solid line indicated the dispersion curve of the edge state, and the gray area was marked according to the frequency intervals of the corner states as shown in Fig. 9. Note that, in Figs. 9(a) and 9(b), frequency ranges of the zigzag edge states and corner states match the eigenspectra of Figs. 4(b) and 4(e) in the main text. A similar rule of valley selection for corner states applies as in

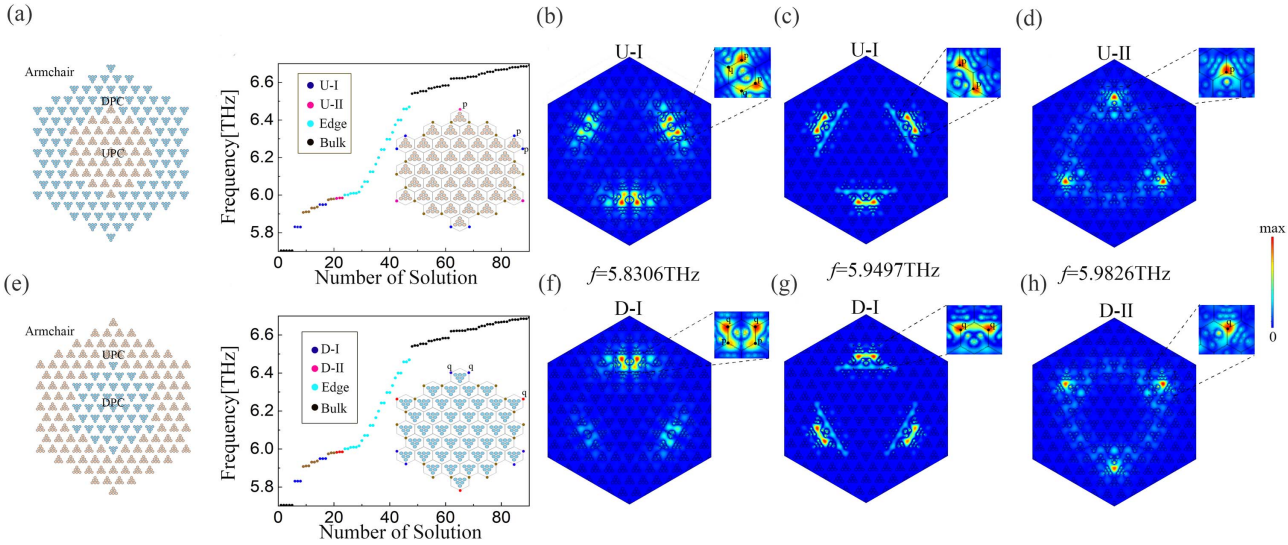

Fig. 8. Dual-polarization models (UPC and DPC) select the corner state in the armchair boundary. (a) Left panel: Schematic structure for armchair edges with the DPC surrounding the UPC. Right panel: UPC eigenfrequency distribution of the bulk-edge-corner states. The red and blue dots indicate the positions of U-I and U-II corner states, and the brown dots indicate those of corner states. (b)–(d) Electric-field distribution of U-I and U-II corner states. (e) Left panel: Schematic for armchair edges with the UPC surrounding the DPC. Right panel: DPC eigenfrequency distribution of the bulk-edge-corner states. The red and blue dots indicate the positions of D-I and D-II corner states, and the brown dots indicate those of the corner states. (f)–(h) Electric-field distribution of D-I and D-II corner states. Note that the U-I corner states both appear at the same p positions in (b) and (c), and the D-I corner states appear at the same q positions in (g) and (h).

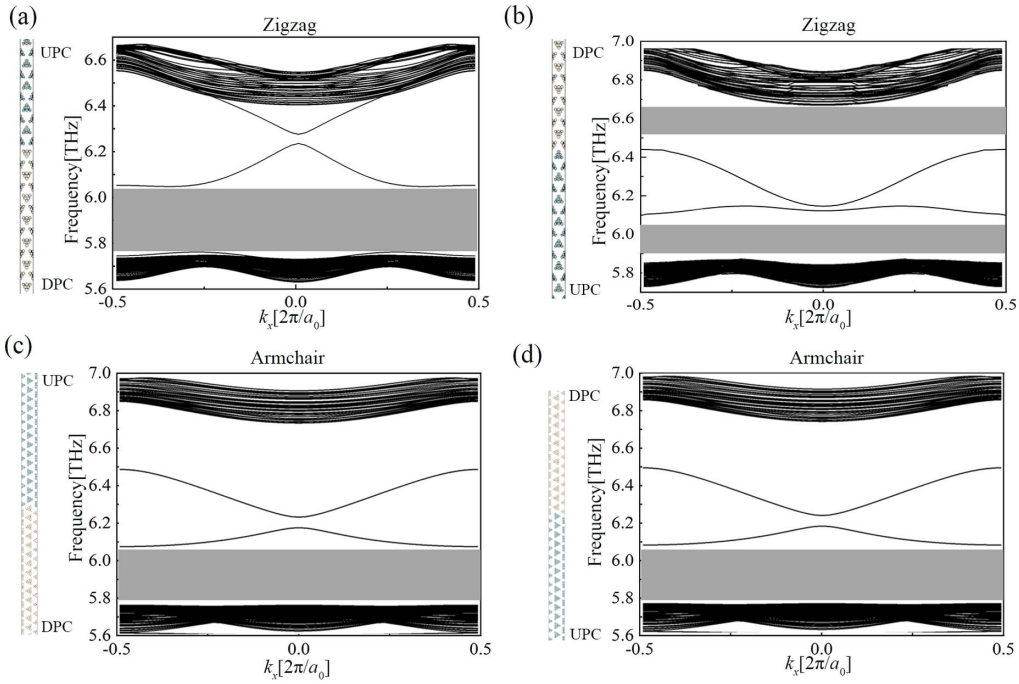

Fig. 9. Projection bands for the zigzag and armchair interfaces between the UPC and the DPC and its unit-cell layout. (a) The corner state of the zigzag interface appears below the edge state. (b) The corner state of the zigzag interface appears above and below the edge state. (c) and (d) The corner state of the armchair interface all appears below the edge state and the gray area is marked according to the frequency interval of corner states. Note that we omit two edge dispersion curves in (c) and (d) resulting from irrelevant interaction due to perfect electrical conductor (PEC) boundaries along the y direction.

Figs. 9(c) and 9(d). Because the two armchair-type interfaces have the same shape, the edge state transmission is also the same [26].

APPENDIX G: TRANSPORT OF VALLEY EDGE STATES

In order to further verify the edge-transmission features of our design, we test five boundary types for waveguides and use the chiral OAM source in Figs. 10(a)–10(e). It was shown that the zigzag and the armchair boundaries were able to host scatteringless states. Hereby, we define transmission efficiency in Figs. 10(a), 10(b), and 10(d) as

$$T\,(\mathrm{dB}) = 10\log_{10}\frac{P_{\mathrm{out}}}{P_{\mathrm{in}}} = 10\log_{10}\frac{\iint p_{\mathrm{out}}\,\mathrm{d}S}{\iint p_{\mathrm{in}}\,\mathrm{d}S}, \tag{G1}$$

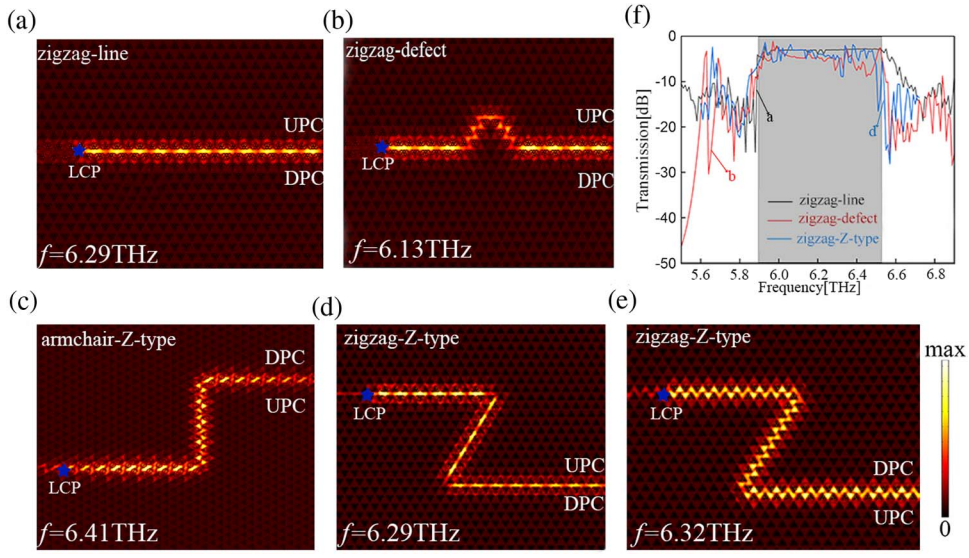

Fig. 10. Defected waveguides of various shapes excited by an OAM source, which is an LCP OAM one. (a) In-line waveguide along the zigzag interface; (b)–(e) curved waveguides along the zigzag interface; (f) transmission spectrum for three zigzag edge states (a), (b), and (d) [cf. also the edge mode of Fig. 9(a)], which gives a wide bandwidth between 5.9 and 6.5 THz.

where p_{in} and p_{out} are the planar densities of power flow in the input and output regions, respectively. By calibrating transmission spectra around the bandgap of the zigzag-type waveguide as shown in Fig. 10(f), we found that the topologically protected edge state was also highly efficient in transmission therein.

Funding. Young Scientists Fund (NSFC11804087, NSFC11704106); National Natural Science Foundation of China (NSFC12047501, NSFC12074108, NSFC41974195); Fundamental Research Funds for the Central Universities (CCNU19TS073, CCNU20GF004); Hongque Innovation Center (HQ202104001); Hubei University (030-090105, A201508); Science and Technology Department of Hubei Province (2018CFB148).

Acknowledgment. R.Z., H.L., Y.W., Z.L. and Z.Y. thank the Central China Normal University. Y.L. and D.-H.X. thank the Chutian Scholars Program in Hubei Province, the Hubei Key Laboratory of Ferro- and Piezoelectric Materials and Devices (Hubei University), and the Institute of Physics Carers' Funds (IOP, U.K.). R.Z. and D.-H.X. proposed the idea. R.Z. performed the calculation, produced all the figures, and wrote the paper draft. H.L. and Y.L. led the project and revised the whole paper thoroughly. R.Z., Y.L. and D.-H.X. put inputs together from all other coauthors in the paper revision.

Disclosures. The authors declare no conflicts of interest.

Data Availability. Data underlying the results presented in this paper are not publicly available at this time but may be obtained from the authors upon reasonable request.

REFERENCES

1. F. D. M. Haldane and S. Raghu, "Possible realization of directional optical waveguides in photonic crystals with broken time-reversal symmetry," Phys. Rev. Lett. **100**, 013904 (2008).
2. Z. Wang, Y. D. Chong, J. D. Joannopoulos, and M. Soljačić, "Reflection-free one-way edge modes in a gyromagnetic photonic crystal," Phys. Rev. Lett. **100**, 013905 (2008).
3. A. B. Khanikaev, S. H. Mousavi, W. K. Tse, M. Kargarian, A. H. MacDonald, and G. Shvets, "Photonic topological insulators," Nat. Mater. **12**, 233–239 (2013).
4. J. Y. Lu, C. Y. Qiu, M. Z. Ke, and Z. Y. Liu, "Valley vortex states in sonic crystals," Phys. Rev. Lett. **116**, 093901 (2016).
5. L. H. Wu and X. Hu, "Scheme for achieving a topological photonic crystal by using dielectric material," Phys. Rev. Lett. **114**, 223901 (2015).
6. R. Zhou, H. Lin, Y. Liu, X. T. Shi, R. X. Tang, Y. J. Wu, and Z. H. Yu, "Topological edge states of kekulé-type photonic crystals induced by a synchronized rotation of unit cells," Phys. Rev. A **104**, L031502 (2021).
7. Q. L. Chen, L. Zhang, M. J. He, Z. J. Wang, X. Lin, F. Gao, B. Yang, Y. H. Zhang, and H. S. Chen, "Valley-hall photonic topological insulators with dual-band kink states," Adv. Opt. Mater. **7**, 1900036 (2019).
8. L. Zhang, Y. H. Yang, M. J. He, H. X. Wang, Z. J. Yang, E. P. Li, F. Gao, B. Zhang, J. H. Jiang, and H. S. Chen, "Valley kink states and topological channel intersections in substrate-integrated photonic circuitry," Laser Photon. Rev. **13**, 1900159 (2019).
9. J. Y. Lu, C. Y. Qiu, L. P. Ye, X. Y. Fan, M. Z. Ke, F. Zhang, and Z. Y. Liu, "Observation of topological valley transport of sound in sonic crystals," Nat. Phys. **13**, 369–374 (2016).
10. J. W. Dong, X. D. Chen, H. Zhu, Y. Wang, and X. Zhang, "Valley photonic crystals for control of spin and topology," Nat. Mater. **16**, 298–302 (2017).
11. W. A. Benalcazar, A. Bernevig, and T. L. Hughes, "Quantized electric multipole insulators," Science **357**, 61–66 (2017).
12. W. A. Benalcazar, B. A. Bernevig, and T. L. Hughes, "Electric multipole moments, topological multipole moment pumping, and chiral hinge states in crystalline insulators," Phys. Rev. B **96**, 245115 (2017).
13. Z. D. Song, Z. Fang, and C. Fang, "$(d-2)$-dimensional edge states of rotation symmetry protected topological states," Phys. Rev. Lett. **119**, 246402 (2017).
14. F. Schindler, M. Cook Ashley, G. Vergniory Maia, Z. Wang, S. P. Parkin Stuart, B. A. Bernevig, and T. Neupert, "Higher-order topological insulators," Sci. Adv. **4**, eaat0346 (2018).
15. W. A. Benalcazar, T. Li, and T. L. Hughes, "Quantization of fractional corner charge in C_n-symmetric higher-order topological crystalline insulators," Phys. Rev. B **99**, 245151 (2019).
16. M. S. Kirsch, Y. Q. Zhang, M. Kremer, L. J. Maczewsky, S. K. Ivanov, Y. V. Kartashov, L. Torner, D. Bauer, A. Szameit, and M. Heinrich, "Nonlinear second-order photonic topological insulators," Nat. Phys. **17**, 995–1000 (2021).
17. B. Y. Xie, H. F. Wang, H. X. Wang, X. Y. Zhu, J. H. Jiang, M. H. Lu, and Y. F. Chen, "Second-order photonic topological insulator with corner states," Phys. Rev. B **98**, 205147 (2018).
18. H. R. Kim, M. S. Hwang, D. Smirnova, K. Y. Jeong, Y. Kivshar, and H. G. Park, "Multipolar lasing modes from topological corner states," Nat. Commun. **11**, 5758 (2020).
19. X. Xi, X. M. Li, K. P. Ye, H. B. Wu, J. Chen, and R. X. Wu, "Dual-polarization topological phases and phase transition in magnetic photonic crystalline insulator," New J. Phys. **23**, 083042 (2021).
20. F. Liu and K. Wakabayashi, "Novel topological phase with a zero Berry curvature," Phys. Rev. Lett. **118**, 076803 (2017).
21. F. Liu, H. Y. Deng, and K. Wakabayashi, "Topological photonic crystals with zero Berry curvature," Phys. Rev. B **97**, 035442 (2018).
22. X. T. He, E. T. Liang, J. J. Yuan, H. Y. Qiu, X. D. Chen, F. L. Zhao, and J. W. Dong, "A silicon-on-insulator slab for topological valley transport," Nat. Commun. **10**, 1 (2019).
23. Y. Mao, Y. Liu, and H. Lin, "Angular momenta in fields from a rotational mechanical antenna," J. Phys. Commun. **5**, 125012 (2021).
24. X. D. Chen, X. T. He, and J. W. Dong, "All-dielectric layered photonic topological insulators," Laser Photon. Rev. **13**, 1900091 (2019).
25. M. Y. Li, D. Zhirihin, M. Gorlach, X. Ni, D. Filonov, A. Slobozhanyuk, A. Alù, and A. B. Khanikaev, "Higher-order topological states in photonic kagome crystals with long-range interactions," Nat. Photonics **14**, 89–94 (2020).
26. X. J. Zhang, M. H. Liu, L. Lu, and Y. F. Chen, "Valley-selective topological corner states in sonic crystals," Phys. Rev. Lett. **126**, 156401 (2021).
27. A. Neto, F. Guinea, N. Peres, K. S. Novoselov, and A. K. Geim, "The electronic properties of graphene," Rev. Mod. Phys. **81**, 109–162 (2009).
28. J. R. Schaibley, H. Y. Yu, G. Clark, P. Rivera, J. S. Ross, K. L. Seyler, W. Yao, and X. D. Xu, "Valleytronics in 2D materials," Nat. Rev. Mater. **1**, 16055 (2016).
29. L. Lu, J. D. Joannopoulos, and M. Soljačić, "Topological photonics," Nat. Photonics **8**, 821–829 (2014).
30. X. D. Chen, W. M. Deng, J. C. Lu, and J. W. Dong, "Valley-controlled propagation of pseudospin states in bulk metacrystal waveguides," Phys. Rev. B **97**, 184201 (2018).
31. Z. K. Lin and J. H. Jiang, "Dirac cones and higher-order topology in quasi-continuous media," arXiv:2112.00352 (2021).
32. X. D. Chen, F. L. Zhao, M. Chen, and J. W. Dong, "Valley-contrasting physics in all-dielectric photonic crystals: orbital angular momentum and topological propagation," Phys. Rev. B **96**, 020202 (2017).
33. E. Khalaf, "Higher-order topological insulators and superconductors protected by inversion symmetry," Phys. Rev. B **97**, 205136 (2018).
34. J. L. Liu, W. M. Ye, and S. Zhang, "Pseudospin-induced chirality with staggered optical graphene," Light Sci. Appl. **5**, e16094 (2016).
35. I. A. Litvin, A. Dudley, and A. Forbes, "Poynting vector and orbital angular momentum density of superpositions of bessel beams," Opt. Express **19**, 16760–16771 (2011).

36. H. X. Wang, L. Liang, B. Jiang, J. H. Hu, X. C. Lu, and J. H. Jiang, "Higher-order topological phases in tunable C_3 symmetric photonic crystals," arXiv:2102.11388 (2021).
37. M. P. Makwana and G. Chaplain, "Tunable three-way topological energy-splitter," Sci. Rep. **9**, 18939 (2019).
38. Z. G. Geng, Y. G. Peng, P. Q. Li, Y. X. Shen, D. G. Zhao, and X. F. Zhu, "Mirror-symmetry induced topological valley transport along programmable boundaries in a hexagonal sonic crystal," J. Phys. Condens. Matter **31**, 245403 (2019).
39. F. Gao, H. R. Xue, Z. Y. Yang, K. F. Lai, Y. Yu, X. Lin, Y. D. Chong, G. Shvets, and B. Zhang, "Topologically protected refraction of robust kink states in valley photonic crystals," Nat. Phys. **14**, 140–144 (2018).
40. Y. H. Yang, Y. Yamagami, X. B. Yu, P. Pitchappa, J. Webber, B. Zhang, M. Fujita, T. Nagatsuma, and R. Singh, "Terahertz topological photonics for on-chip communication," Nat. Photonics **14**, 446–451 (2020).
41. L. Zhang, Y. H. Yang, Z. Jiang, Q. L. Chen, Q. H. Yan, Z. Y. Wu, B. Zhang, J. Huangfu, and H. S. Chen, "Demonstration of topological wireless power transfer," Sci. Bull. **66**, 974–980 (2021).
42. S. Q. Wu, B. Jiang, Y. Liu, and J. H. Jiang, "All-dielectric photonic crystal with unconventional higher-order topology," Photon. Res. **9**, 668–677 (2021).